PLOS ONE

RESEARCH ARTICLE

Enhanced hydrogen evolution from CuO_x-C/TiO_2 with multiple electron transport pathways

Xiuying Huang, Meng Zhang, Runze Sun, Gaoyuan Long, Yifan Liu, Weirong Zhao*

Department of Environmental Engineering, Zhejiang University, Hangzhou, China

* wrzhao@vip.163.com

Citation: Huang X, Zhang M, Sun R, Long G, Liu Y, Zhao W (2019) Enhanced hydrogen evolution from CuO_x-C/TiO_2 with multiple electron transport pathways. PLoS ONE 14(4): e0215339. https://doi.org/10.1371/journal.pone.0215339

Editor: Satya Pal Nehra, University of California Santa Barbara, California, USA

Received: January 22, 2019

Accepted: March 29, 2019

Published: April 15, 2019

Data Availability Statement: All relevant data are within the manuscript, Supporting Information files, and on Figshare: http://dx.doi.org/10.6084/m9.figshare.7951724.

Funding: This work has been partially supported by the National Natural Science Foundation of China (Grant No. 51278456 and 51778564) to WZ. The funders had no role in study design, data collection and analysis, decision to publish, or preparation of the manuscript.

Competing interests: The authors have declared that no competing interests exist.

Abstract

Titanium dioxide nanoparticles co-modified with CuO_x ($0 \leq x \leq 2$) and carbonaceous materials were prepared with a simple hydrolysis and photo-reduction method for photocatalytic hydrogen generation. SEM/TEM and XPS analysis indicated that the carbonaceous materials were mostly coated on the TiO_2 surface and clearly revealed that the Cu species exhibited multivalence states, existing as CuO_x ($0 \leq x \leq 2$). The optimal catalyst showed a 56-fold enhanced hydrogen evolution rate compared with that of the pure C/TiO_2 catalyst. Further, an intensive multiple electron transfer effect originating from CuO_x and the carbonaceous materials is proposed to be responsible for the elevated photoactivity. CuO_x species serve as electron donors facilitating charge carrier transfer and proton reduction sites. The carbonaceous materials function as the "bridge" that transfers the electrons of TiO_2 to the CuO_x species, which provides a new route for electron transfer and reinforces the effect of CuO_x as a co-catalyst. In this study, the CuO_x and C co-modified TiO_2 catalyst was prepared with multiple electron transport pathways and enhanced hydrogen production evolution, which provides a deep understanding for the design of co-catalyst-based photocatalysts.

1 Introduction

Hydrogen, as an efficient, renewable and clean energy source, is considered to be one of the best fuels for the future [1, 2]. Hence, photocatalytic hydrogen production with semiconductors has been regarded as a promising strategy for its mild reaction conditions, and cost-effectiveness [3, 4]. Among the various studied photocatalysts, titanium dioxide (TiO_2) has received tremendous attention for photocatalytic hydrogen evolution owing to its suitable conduction and valence bands edge position, as well as its characteristics of nontoxicity, low cost, and photocorrosion resistance [5, 6]. However, the undesirable charge carrier recombination and the inferior solar light utilization efficiency of TiO_2, which leads to the low photocatalytic hydrogen generation efficiency, restrict their photochemical applications [7]. It is a hot issue to develop an effective method to overcome the intrinsic limitation.

Co-catalysts [8–10] have been developed to enhance charge carrier separation and activate redox reactions on catalyst surfaces. Noble metals such as Pt [11] and Pd [12] are often used as co-catalysts for TiO_2, increasing the hydrogen evolution rate significantly. Noble metals can accept

electrons from a semiconductor due to its high work function, which facilitates electron-hole separation. Their high-activity surfaces can act as active sites for hydrogen evolution. However, noble metals are hardly employed for practical applications due to their scarcity and valuableness.

As an alternative, transition metals (e.g., Ni, Cu, Co) [13–15] have emerged as an effective co-catalyst for H_2 evolution. Among them, copper is one of the most promising candidates [16–18]. Ohno et al. [19] prepared TiO_2 modified with Cu and other ions (iron(III), nickel(II) and chromium(III) ions), revealing that metal ions can serve as both electron acceptors and donors based on a double-beam photoacoustic spectroscopy measurement. Characterization experiments and theoretical calculations confirmed this conclusion [20]. In addition, Nosaka et al. [21] proposed an interfacial charge transfer (IFCT) mechanism for the Cu/TiO_2 in which transition metal ions can function as a trap for excited electrons to decrease recombination. The authors believed that Cu(I) can be formed by the photoexcited electron reduction of Cu (II), and Cu(II)-grafted samples are capable of reducing O_2 to $O_2^{\cdot-}$. The multivalent states of Cu are regarded as the active species for the photoreaction. Our group fabricated Cu(II) nanodot doped nanosheet TiO_2 in a previous report [22], in which H_2 evolution increased 25-fold due to the multiple charge-transfer pathways. Here, we introduced another species co-modified with Cu and managed to raise the hydrogen quantity.

Carbonaceous materials, such as carbon nanotubes (CNTs) [23] and graphene [24], have been considered as another kind of efficient co-catalyst for photocatalytic applications. Xiang et al. [25] prepared graphene-modified titania nanosheets and a 41-time enhancement of H_2 evolution rate was observed. The authors revealed that graphene can facilitate electron transfer by accepting photoelectrons as well as functioning as active sites for the photocatalytic reaction. A similar mechanism is also applicable to CNT-TiO_2 composites [26].

TiO_2 co-modified with transition metals and nonmetal carbonaceous materials is a new route to facilitate the charge carrier separation and increase photoactivity. Zhang et al. [27] prepared a Cu-grafted TiO_2/graphene photocatalyst for efficient phenol degradation, in which graphene provides a new electron transfer route and enhances the co-catalyst effect for superoxide radical generation.

Inspired by the above achievements, we have prepared a foam-like CuO_x-C/TiO_2 catalyst via a facile hydrolysis and photo-reduction method for photocatalytic hydrogen generation. By controlling the amount of water, the titanium precursor can be hydrolyzed completely. Thus, the carbonaceous materials originated from the calcination process without an external carbon precursor. The formation of carbonaceous materials and Cu species were systematically explored. The results demonstrated that carbonaceous materials serve as electron conductors to enhance the co-catalyst effect of CuO_x, inducing multiple electron transfer pathways for photocatalytic hydrogen generation.

2 Experiment section

2.1 Materials

Tetrabutyl titanate ($Ti(OBu)_4$), copper chloride ($CuCl_2.2H_2O$), ethanol (C_2H_5OH), and glycerol ($C_3H_8O_3$) were purchased from Sinopharm Chemical Reagent Co., Ltd, China. All reagents were analytical grade and used without further purification. Deionized water was used for all experiments.

2.2 Catalyst preparation

C/TiO_2 (CT) photocatalysts were synthesized by a facile sol-gel method. Typically, 5.5 mL of deionized water was added to 25 mL of tetrabutyl titanate ($Ti(OBu)_4$) under magnetic stirring for 48 h. The mixture was filtered by a Buchaer funnel and dried in an oven at 80˚C overnight.

The prepared catalyst was denoted as CT. Then, CT samples were calcined at 350˚C, 400˚C, 500˚C and 550˚C for 2 h, respectively. The corresponding dark brown powders were denoted as CTR (R = 350, 400, 500 and 550).

CuO_x-C/TiO_2 was prepared according to a previously published photo-reduction method [28]. A certain amount of CTR catalyst was added to 100 mL of solution containing 5 v% glycerol and a given volume of $CuCl_2$ aqueous solution (0.01mol/L). The mixture was placed to a photocatalytic quartz reactor which was bubbled with Ar for 0.5 h and then irradiated with a 300 W xenon lamp for 2 h under magnetic stirring. After extensive washing, the precipitate was dried at 80˚C overnight and then calcined at 350˚C with a heating rate of 5˚C min^{-1} for 2 h. The prepared powders were denoted as CuO_x-CTR (R = 350, 400, 500 and 550), the Cu/Ti molecule ratio of which is 1%.

2.3 Characterization

The structural characterization of the as-synthesized materials was performed by X-ray diffraction (XRD, PANalytical, Netherlands), and their morphology of them was observed by a scanning electron microscope (SEM, Supra55, Zeiss, Germany), transmission electron microscope (TEM, JEM-2010, JEOL, Japan), and high-resolution TEM, as illustrated in a previous work [22]. Molybdenum support films were used instead of carbon support films for TEM sample preparation. Element analysis (EA), X-ray photoelectron spectroscopy (XPS, Escalab 250Xi, Thermo, England) and UV–vis diffuse reflectance spectroscopy (UV–vis DRS, TU-1901, Pgeneral, Beijing, China) were used to monitor the components and surface chemical states of the prepared photocatalysts. The crystallization behavior was recorded using a NETZSCH STA490PC TG-DSC instrument with the temperature ranging from room temperature to 900˚C. Specific surface area of the photocatalysts were measured by the Brunauer–Emmett–Teller (BET) method with automatic analyzer (3H-2000PS2, Beishide, Beijing, China) and the pore-size distributions were determined by using absorption curves and the Barrett–Joyner–Halenda (BJH) method.

To explore the charge carriers, photoluminescence emission spectra were measured at room temperature with a fluorescence spectrophotometer (FLS920, Edinburgh, England) using a 325 nm wavelength laser as the excitation source. In addition, all photoelectrochemical measurements (photocurrent densities vs time curves I–t, Nyquist plots and Tafel spectra) were conducted with a three-electrode workstation (CHI 660D, Shanghai, China).

2.4 Photocatalytic activity experiment

The photocatalytic activity experiment was performed in a top-irradiation jacketed quartz photoreactor with water flowing through to maintain a constant temperature (30 ± 1˚C). In a typical reaction, 50 mg of photocatalyst was dispersed in 100 mL of 5 v% glycerol with magnetic stirring. The catalyst suspension was first degassed with an Ar stream for an hour. Subsequently, the solution inside the reactor was irradiated by a 300 W xenon lamp (CEL-HXUV300, Aulight, Beijing, China). The generated H_2 was detected every half hour by a gas chromatograph (Fuli 9790, Zhejiang, China) equipped with a thermal conductivity detector using Ar as carrier gas. Another gas chromatograph with a flame ionization detector (Fuli 9790, Zhejiang, China) was used to determine the evolution of CO and CO_2.

3 Results and discussions

3.1 Morphology and crystal structure

X-ray powder diffraction was used to analyze the crystal structures of CT, CT400 and CuO_x-CT400. As shown in Fig 1, the XRD pattern of the CT sample without thermal treatment

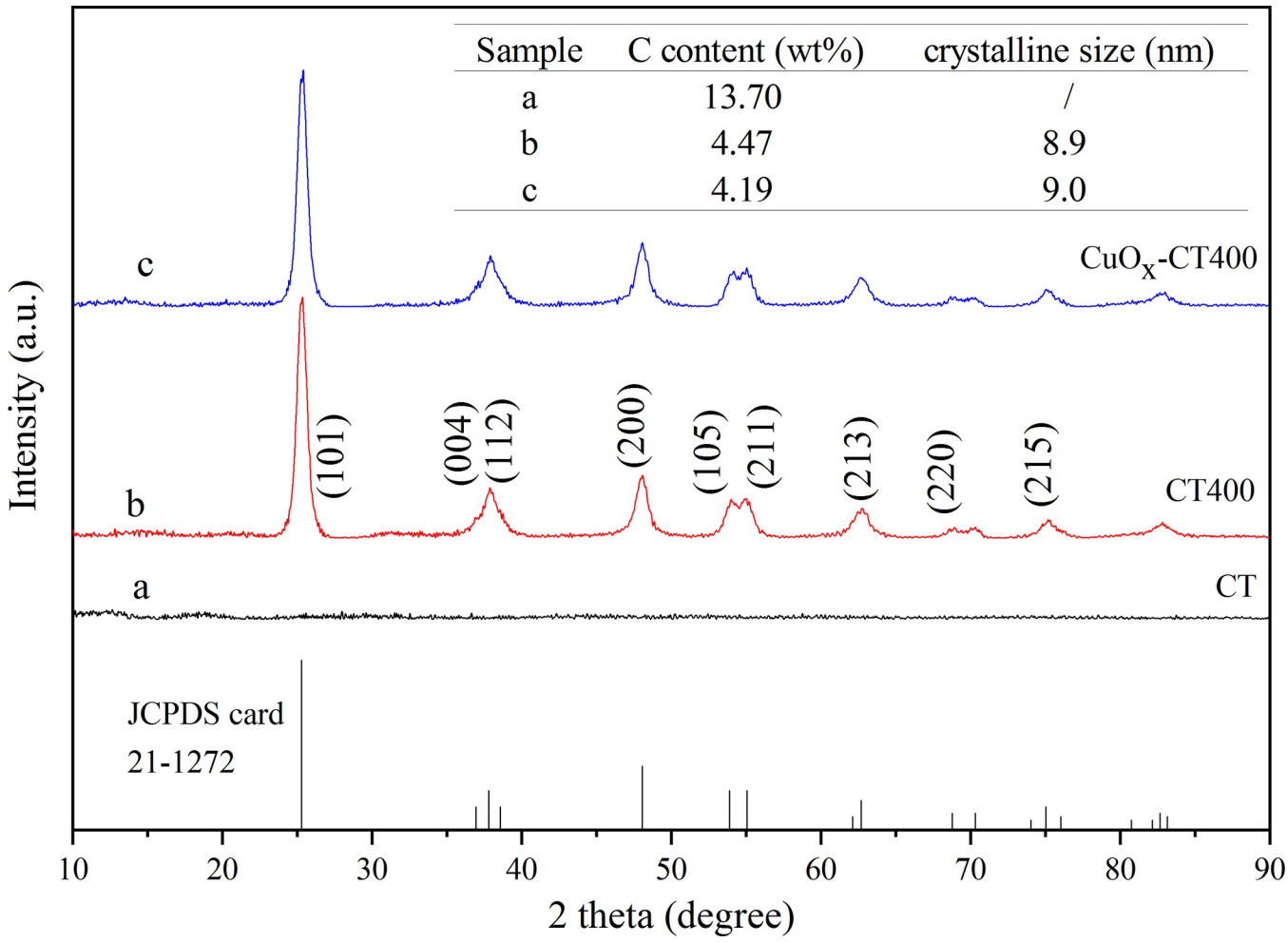

Fig 1. XRD patterns of the studied samples.

https://doi.org/10.1371/journal.pone.0215339.g001

shows broad amorphous features and no peaks indicative of crystalline phases. After a 400˚C treatment for 2 h, the CT400 exhibits characteristic peaks at 25.281˚, 37.800˚, 38.575˚, 48.050˚, 53.890˚, 55.060˚, 62.121˚, 70.311˚, and 75.032˚ corresponding to anatase TiO_2 (JCPDS 21–1272) [22]. After CuO_x modification, the spectrum exhibits a similar peak shape, suggesting that the addition of Cu species did not change the crystal form. Moreover, the average grain size of CT400 was estimated to be approximately 9 nm by using Jade 6.0 and Scherrer's formula [29] from the XRD data.

To investigate the thermostability and components of the CT catalyst, thermogravimetric analysis was conducted. As it demonstrated in Fig 2, C/TiO_2 catalyst shows an approximately 5% weight loss when heated to 100˚C, suggesting water evaporation from the catalyst surface [30]. When it gets to 450˚C, the weight loss was 29%, which could be attributed to the partial removal of tetrabutyl titanate hydrolysate bonded in the titanium dioxide. This instability of the sample indicated that C was successfully coated on the surface of TiO_2 at the calculated temperature of 400˚C. From the DSC curves, it is worth noting that a peak of an exothermic reaction appeared at approximately 352˚C indicating a crystal transition of the catalyst from the amorphous to the anatase phase [30]. Crystal conversion is complete at 400˚C, which is consistent with the previous XRD result.

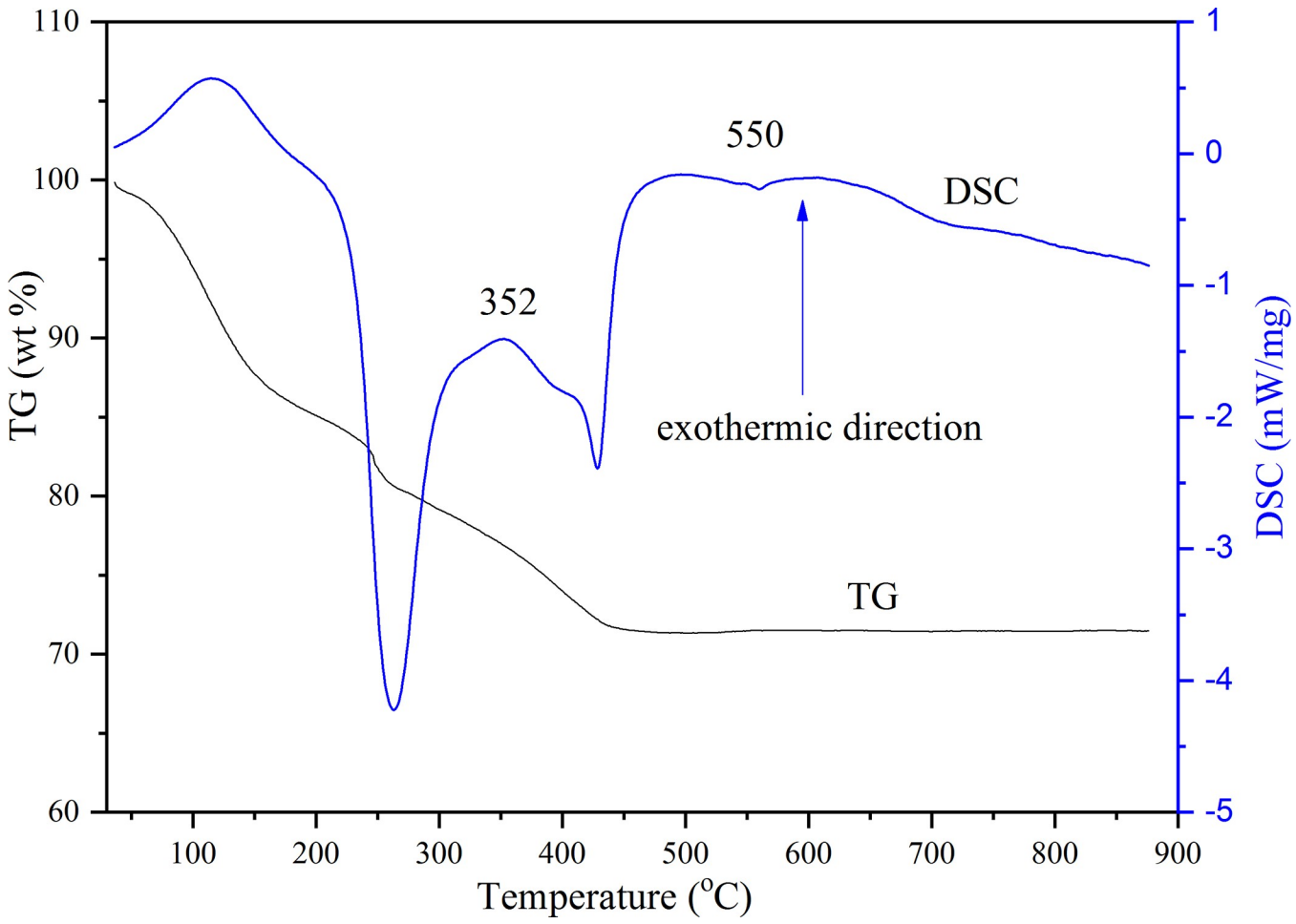

Fig 2. TG-DSC curves of the C/TiO_2 catalyst.

https://doi.org/10.1371/journal.pone.0215339.g002

The microstructures of the C/TiO_2 and CuO_x-C/TiO_2 catalysts were characterized by SEM and TEM. Fig **A in** S1 File shows the SEM images of CT (before calcination). The sample is composed of many aggregated nanosized sphere particles. These spheres result from the hydrolysis of TBOT. To further observe the microstructure, the corresponding TEM images are presented in Fig B in S1 File. The nanosized sphere particles have a distribution in average size of 200 to 300 nm, with smooth edges. From the HR-TEM (Fig B in S1 File), layered amorphous structure on surfaces of the spheres are detected, which could be identified as carbon materials. It is noted that no lattice fringes were found in the catalyst, which suggests that the catalyst remains amorphous. The results are in accordance with the previous XRD pattern.

After heat treatment for 2 h, CT400 shows a similar SEM image with CT in Fig C in S1 File. The spheres show a clear lattice fringe with spacings of 0.352 and 0.238 nm which match well with the 101 and 001 facet of anatase TiO_2, respectively, as seen in Fig 3D [24]. The observed crystallite size of the spheres is approximately 10 nm, which is similar to the one calculated from the XRD results.

The SEM structure of CuO_x-CT400 is presented in Fig D in S1 File. A structure with surface porosity is observed. From the fractured surface structure, the catalyst inside are also full of nanosized particles. As part a and b of Fig 4 show, the HR-TEM images of CuO_x-C/TiO_2 clearly indicate 0.352 nm (101 facet of anatase, JCPDS 21–1272) [24] and 0.232 nm lattice

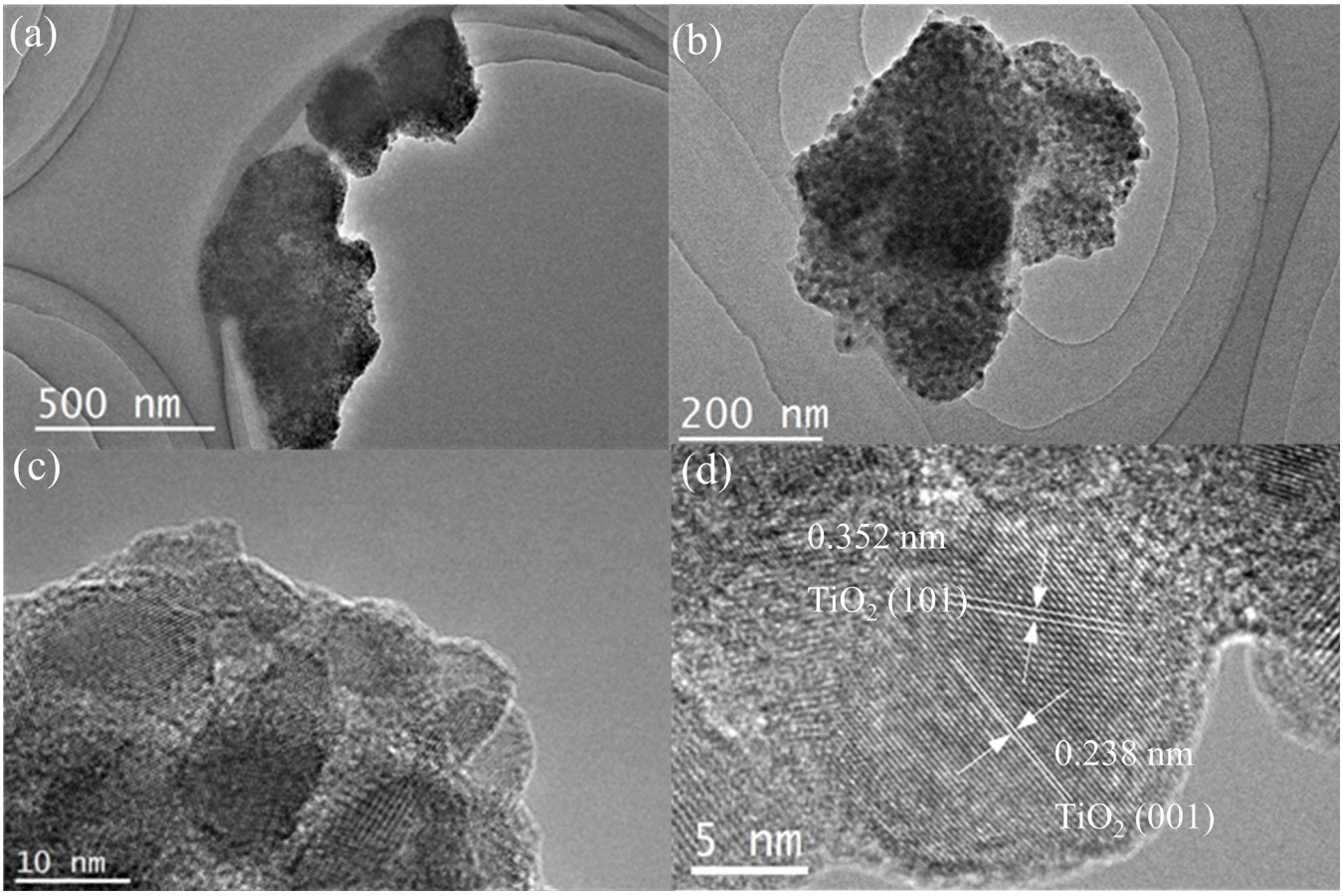

Fig 3. TEM (a, b) and HRTEM (c, d) images of CT400.

https://doi.org/10.1371/journal.pone.0215339.g003

fringes (111 facet of CuO, JCPDS 45–0937) [31]. The EDX spectra (Fig 4D) of the square area (Fig 4C) reveal that Cu, O, Ti, and C coexist in the catalyst. Furthermore, as displayed in the elemental mapping (Fig E in **S1** File), the individual elements of Cu, and C are uniformly distributed on the surface of TiO_2.

Fig 5 shows the nitrogen adsorption-desorption isotherms of CT400 and CuO_x-CT400, both the catalysts exhibit type-IV patterns with H2 hysteresis, ascribed to a typical mesoporous structure [32]. After estimation with the Barret-Joyner-Halenda method, the pore size distribution is shown in the inset of Fig 5. The pore size is mainly in the range of 2.5 to 6.5 nm, which can be attributed to intra-agglomeration of primary particles. It is speculated that the TiO_2 cluster was first formed during the hydrolysis of TBOT as the nucleus and then grown into larger particles with the framework of confined small mesopores [33]. The Brunauer–Emmett–Teller surface area and other parameters of CT400 as well as CuO_x-CT400 are summarized in Table 1. The BET values only show a relatively mild decrease in the presence of Cu species, indicating a possible limited occlusion of the pores of the support by the presence of the co-catalyst.

Fig 6 shows the XPS spectra of CT400 and CuO_x-CT400. In Fig 6A, the binding energy peaks at 459.1 eV and 464.8 eV of CT400 correspond to the Ti $2p_{3/2}$ and Ti $2p_{1/2}$ states with a gap of 5.7 eV, which suggests the presence of the typical Ti^{4+} state [34]. Compared with the previously prepared TiO_2 sample [22] (the Ti 2p3/2 state is at 458.9 eV and the Ti $2p_{1/2}$ state is at 464.6 eV), the CT400 shows a slight 0.2 eV shift to higher binding energy. The result may suggest the surface interaction between the carbonaceous species with the TiO_2 surface. The Ti

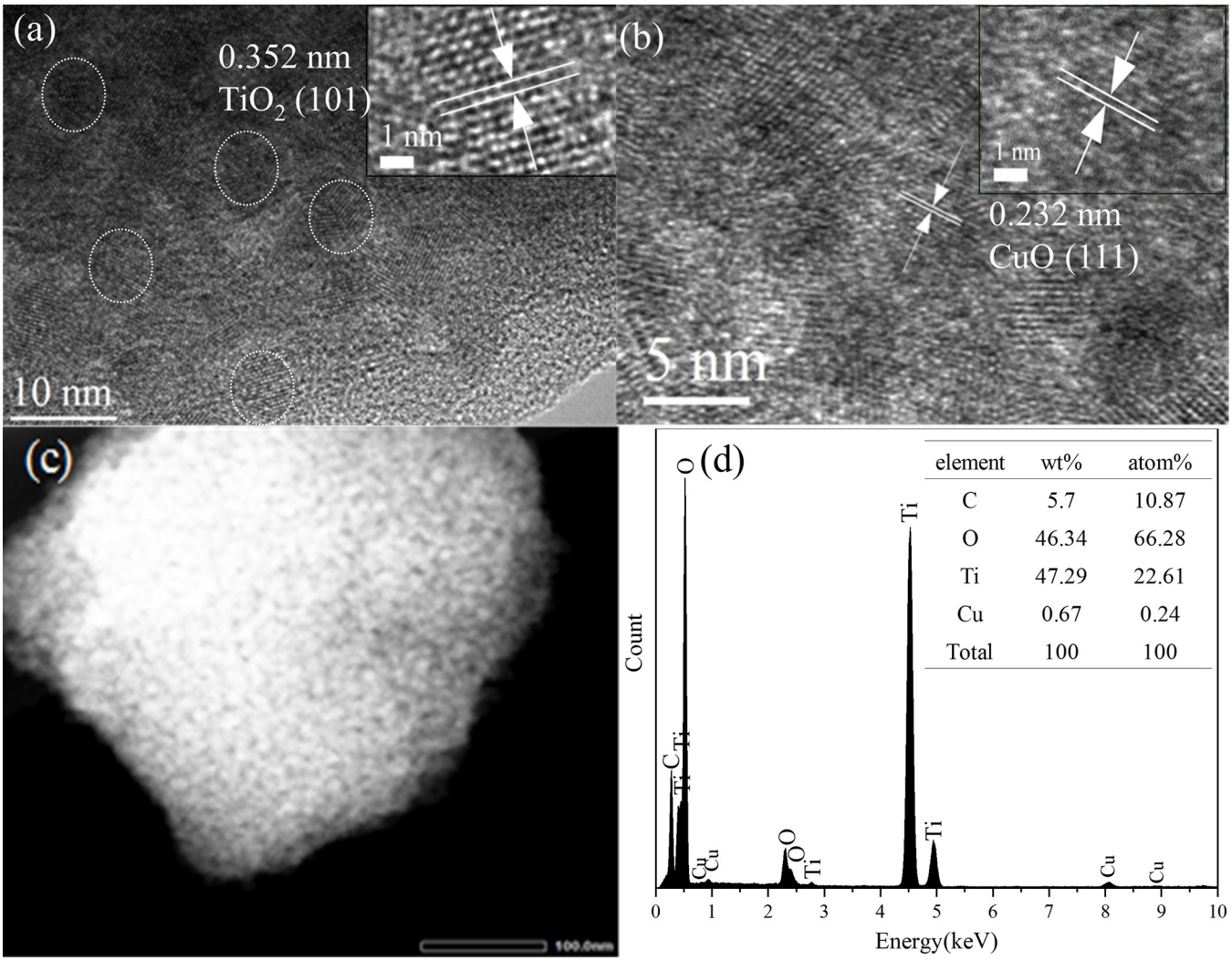

Fig 4. HRTEM images (a-b) of CuO_x-CT400 and HAADF-STEM image (c) and EDX spectrum (d). The insets are the corresponding lattice fringes.

https://doi.org/10.1371/journal.pone.0215339.g004

2p binding energy of CuO_x-CT400 shifts to lower binding energy in contrast with CT400, which indicates charge transfer between the Cu species and C/TiO_2 [31]. The high resolution spectra of Cu $2p_{3/2}$ for CuO_x-CT400 (Fig 6B) exhibit two characteristic peaks at 933.6 and 932.6 eV with XPS-peak-differentiation-imitating analysis. The 933.6 eV peak is attributed to the Cu^{2+} state while the 932.6 eV could be Cu^+ or Cu^0 [35]. To further confirm the exact state of Cu species, the Cu LMM spectra were obtained through AES characterization, as shown in Fig 6C. The broad and asymmetrical Cu LMM spectrum suggests the presence of one more component. After peak fit processing, the three characteristic peaks are 917.2, 916.4, and 918.8eV, corresponding to Cu^{2+}, Cu^+, and Cu^0, respectively [35]. The modified Auger parameter (α') is also a very useful indicator to distinguish between Cu^+ and Cu^0 and is calculated as follows [36]:

$$\alpha' \text{ (eV)} = \text{BE (Cu } 2p_{3/2}\text{)} + \text{KE (Cu LMM)}$$

With this calculation, the values of α' are 1850.8 eV, 1849 eV and 1851.4 eV corresponding to Cu^{2+}, Cu^+, and Cu^0, respectively.

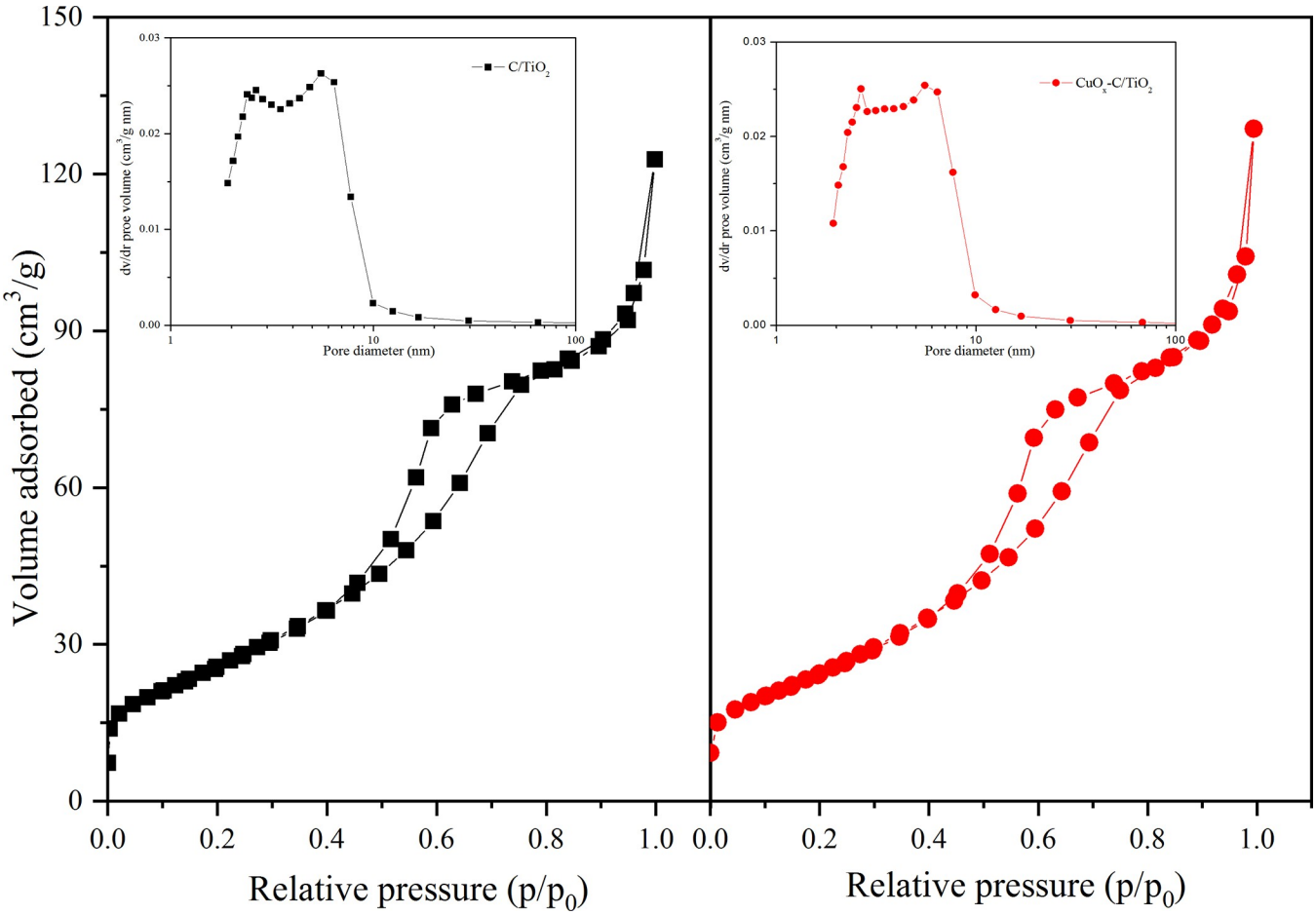

Fig 5. N_2 adsorption–desorption isotherms for CT400 (a) and CuO_x-CT400 (b) and corresponding pore size distribution spectra.

https://doi.org/10.1371/journal.pone.0215339.g005

Fig 6D and 6E shows the high resolution C1s spectra of CT400 and CuO_x-CT400. Three evident peaks at 284.8, 286.3, and 288.7 eV are detected for CT400. The C1s peak at 284.8 eV originated from sp^2 hybridized carbon [37]. The peaks at 286.3 eV and 288.7 eV appear in sample CT400, which are attributed to the oxygen bound species C–O and Ti–O–C, respectively [34, 38]. The peak at 282.1eV with low intensity is close to the C 1s peak related to the binding energy between Ti and C (281.8 eV). Only small amount of C doped into the inner

Table 1. Model parameters of all the photocatalysts based on EIS and BET.

Samples	BET (m^2/g)	Pore volume (mL/g)[a]	Pore diameter (nm)[a]	R_s(Ω/cm^2)[b]	R_{ct}(Ω/cm^2)[c]	$C_{dl} \times 10^8$ (F/cm^2)[d]	$Z_w \times 10^3$ ($S^{0.5}$/Ω cm^2)[e]
CT400	97.3	0.216	6.14	26.2 ± 1.8	122 ± 2.0	0.267 ± 0.088	9.90 ± 0.55
CuO_x-CT400	92.7	0.228	6.57	27.3 ± 0.4	80.6 ± 1.4	10.5 ± 0.30	7.89 ± 0.61

[a]Determined by the BJH method using the nitrogen absorption branch of the isotherm.

[b]The reactivity resistance.

[c]The solution resistance.

[d]The double-layer capacitance.

[e]The Warburg impedance.

https://doi.org/10.1371/journal.pone.0215339.t001

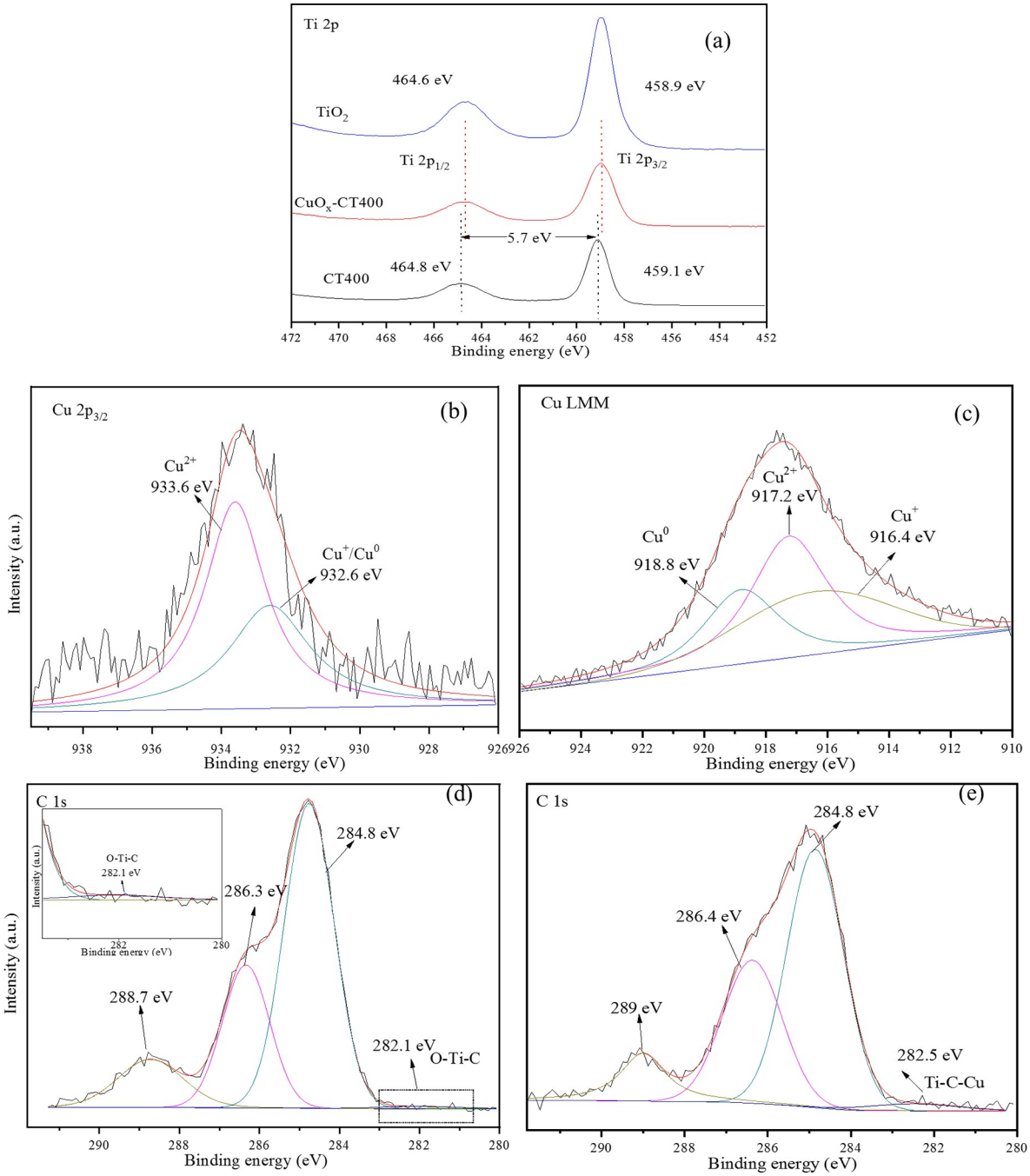

Fig 6. High-resolution XPS spectra of Ti 2p and Cu 2p for CuO_x-CT400 (a, b), Cu LMM spectra for CuO_x-CT400 (c) and C 1s spectra for CT400 (d) and CuO_x-CT400 (e).

https://doi.org/10.1371/journal.pone.0215339.g006

TiO_2 lattice, other carbon may exist as the carbonaceous species formed at the surface of TiO_2 to serve as a conductor. After loading the Cu species, the CuO_x-C/TiO_2 catalyst also exhibits the similar peak shape but a small peak at 282.5 eV, which is close to the Ti-C bond [39] and shifts to higher binding energy, deduced as the Ti-C-Cu bond. Based on the above, it can be concluded that Cu species could be grafted on the carbonaceous materials.

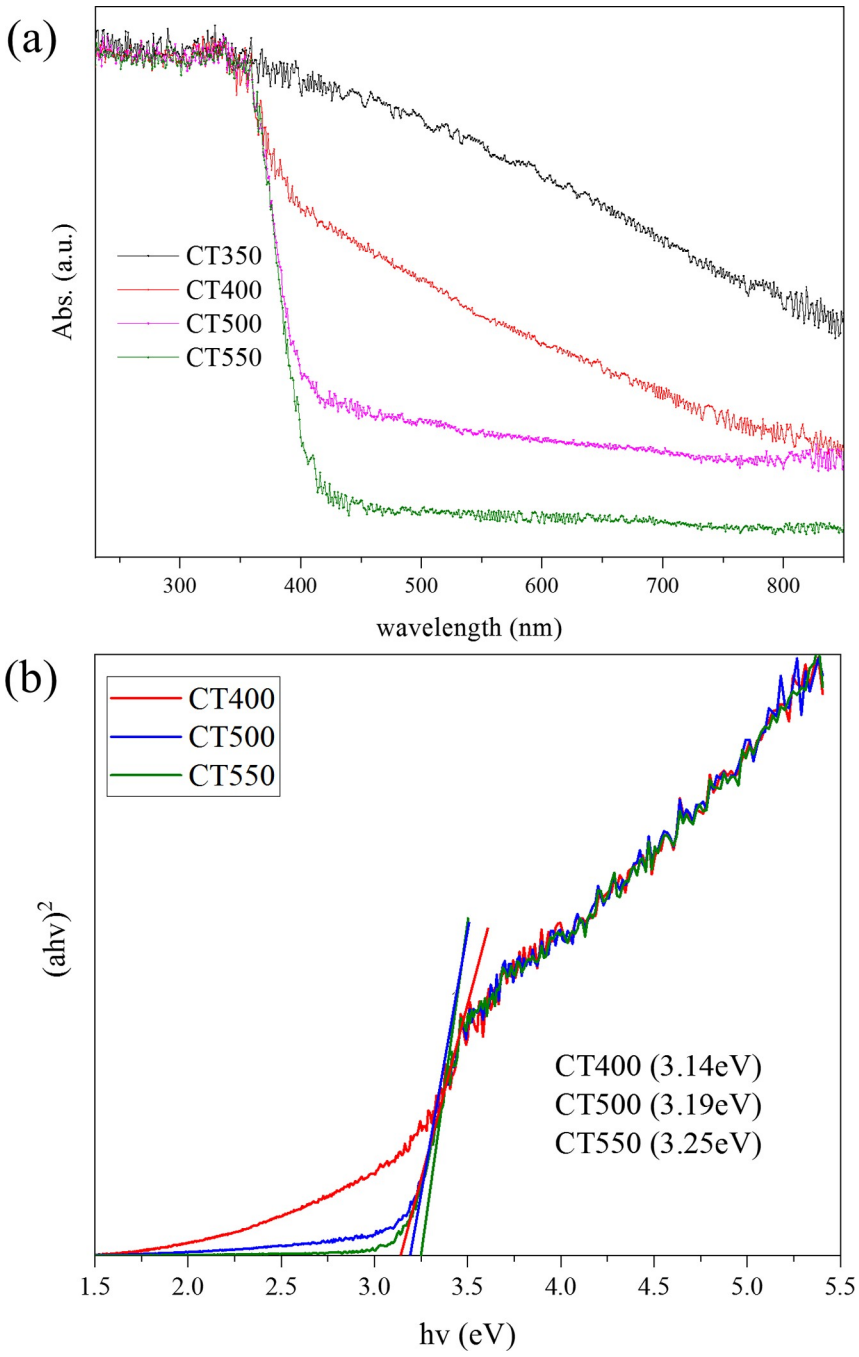

Fig 7. UV-vis diffuse reflectance spectra (a) and the band gap evaluation for linear dependence of $(\alpha hv)^2$ versus hv (b) for the samples.

https://doi.org/10.1371/journal.pone.0215339.g007

3.2 Optical properties

UV-vis diffuse reflectance spectroscopy (DRS) was performed on CT350, CT400, CT500, and CT550 to determine the light harvesting, and the results are shown in Fig 7. In Fig 7A, light harvesting ability exhibits an evident change with different calcination temperatures. Compared to pure TiO_2, the absorption edge of CT350 obviously shifts to the visible light region,

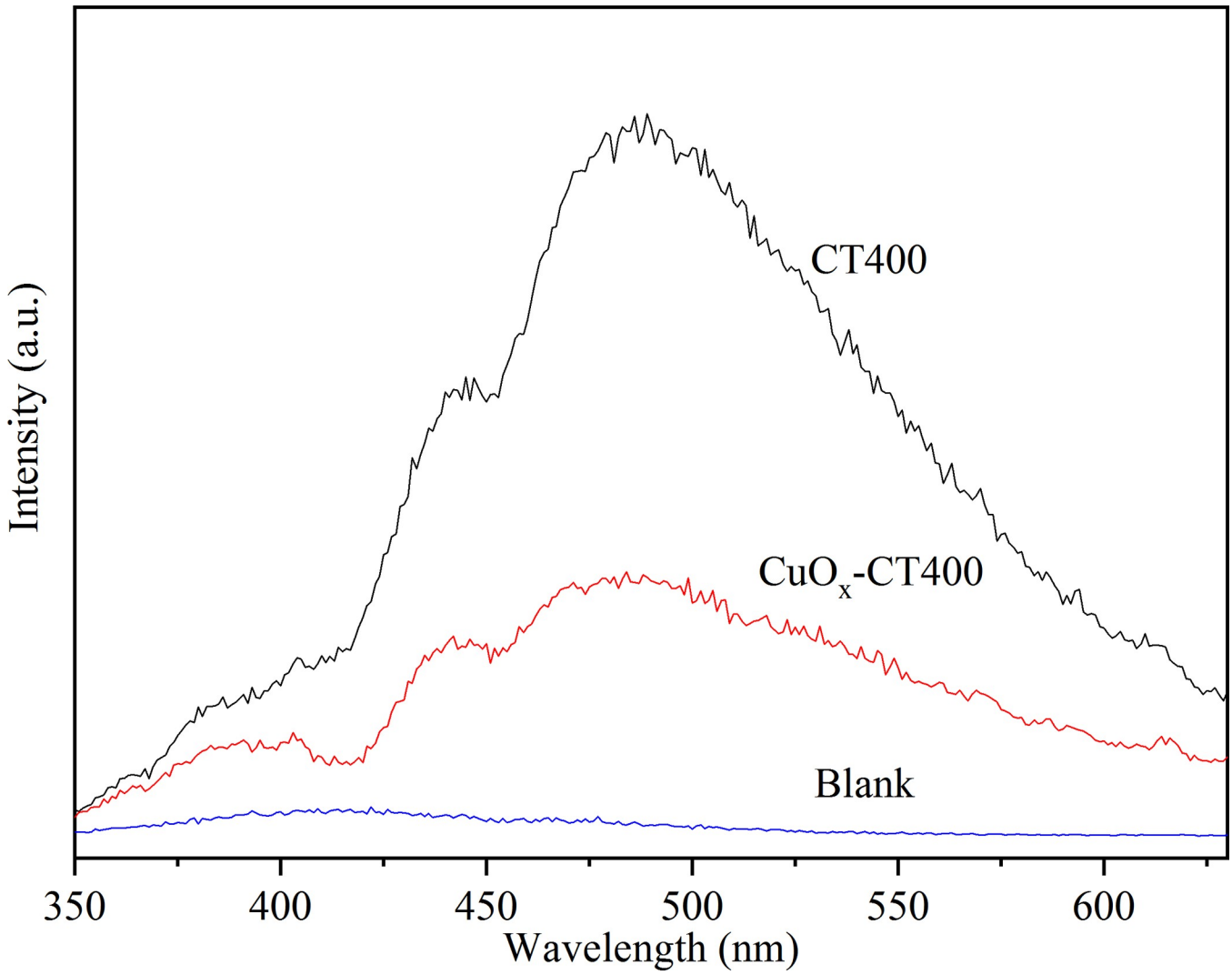

Fig 8. PL spectra of CT400 and CuO_x-CT400.

https://doi.org/10.1371/journal.pone.0215339.g008

which can be attributed to the photo absorption property of the carbonaceous materials absorbed on the TiO_2 surface [40]. The visible absorption of C/TiO_2 decreased significantly with increasing calcination temperature. CT550 exhibits a similar spectrum to the pure TiO_2 lattice. This result proves that carbonaceous species were gradually removed due to the higher temperature, which lead to the decreased absorption of visible light. Notably, the spectra of CT350 exhibit DRS spectra similar to those reported in the literature [38], in which the carbon is coated on the TiO_2 surface. Based on these results, it can be speculated that carbonaceous materials in the CT catalyst mainly adsorb on the TiO_2 surface, which is in accordance with the XPS analysis. As shown in Fig 7B, the direct band gaps of CT400, CT500, CT550 are estimated to be 3.14, 3.19, 3.25 eV, respectively, by using a Tauc plot. They are slightly lower or higher than the reported values of pure anatase TiO_2 [41], which could be attributed to surface defects such as small amounts of carbon impurities [42].

To explore the charge carrier transfer and recombination, photoluminescence emission spectra were employed. As shown in Fig 8, the two curves exhibit similar shapes but vary in fluorescence intensity. There are three peaks (408, 450, and 483 nm) in the wavelength range

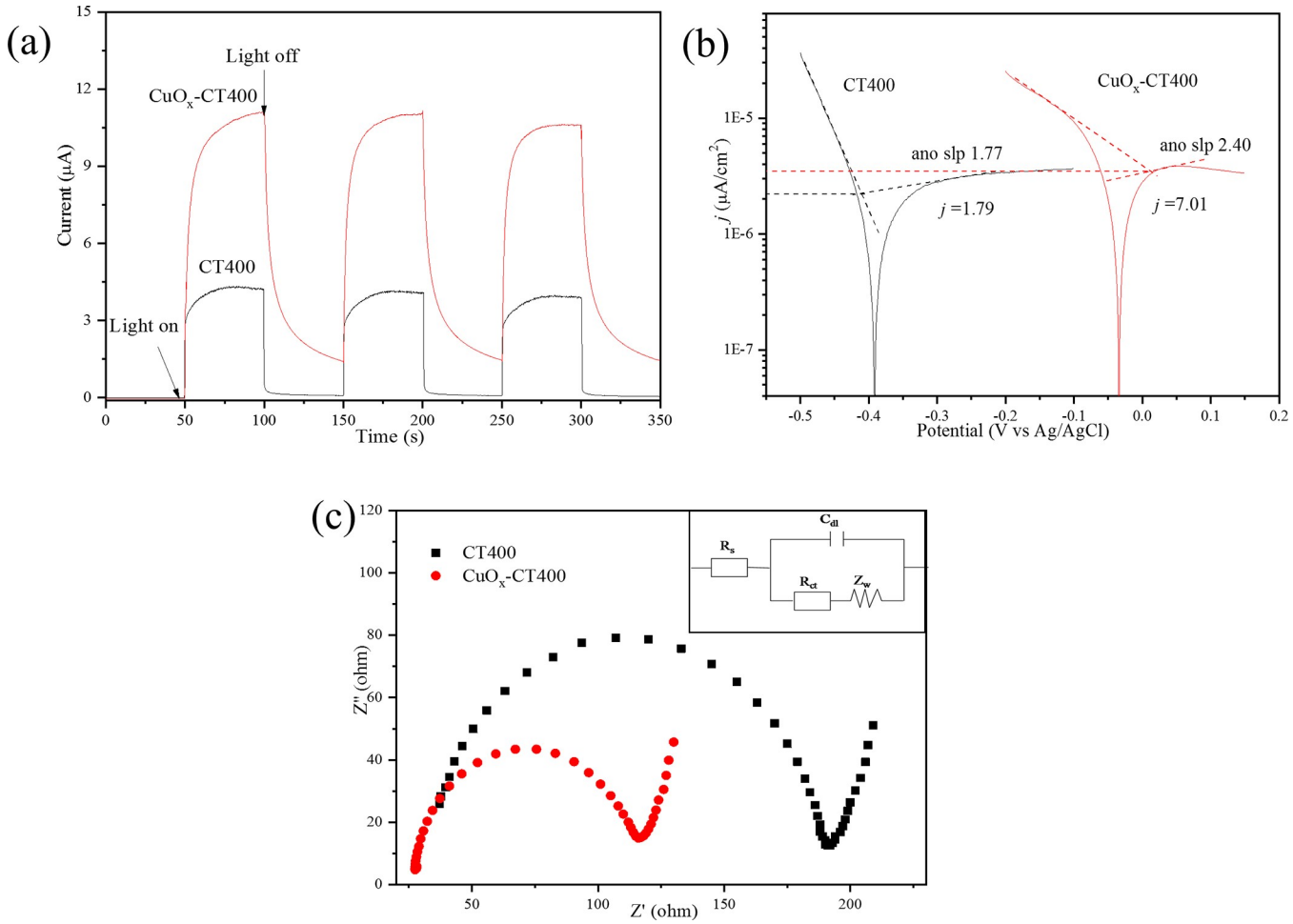

Fig 9. Photoelectrochemical properties of CT400 and CuO_x-CT400 catalyst with i-t spectra (a), Tafel spectra (b), and Nyqusit spectra (c). The inset is the equivalent circuit model.

https://doi.org/10.1371/journal.pone.0215339.g009

of 350–600 nm. The peak of 408 nm is attributed to the interbands PL phenomenon. The two peaks at 450 and 483 nm are ascribed to the band edge free excitons [43]. Overall, the PL intensity decreases with the loading of CuO_x, which indicates that CuO_x favors the transfer of photo-induced electrons and restrains the recombination of photo-induced electrons and holes [44].

3.3 Photoelectrochemical properties

Fig 9 shows the photoelectrochemical properties of the CT400 and CuO_x-CT400 catalysts. The experiment was conducted to reveal the photoexcited electron transfer. As Fig 9A shows, the transient photocurrent increases instantly with the light on and decreases with the light off. The CuO_x-CT400 catalyst exhibits higher photocurrent up to 11.3 μA compared to CT400 with 4.4 μA. Generally, the higher transient photocurrent indicates more electron transfer [45]. It is worth noting that the CuO_x-CT400 catalyst shows an evident spectrum trail when the light is off. The phenomenon is ascribed to complex photoelectron transfer involving the valence state change of Cu species.

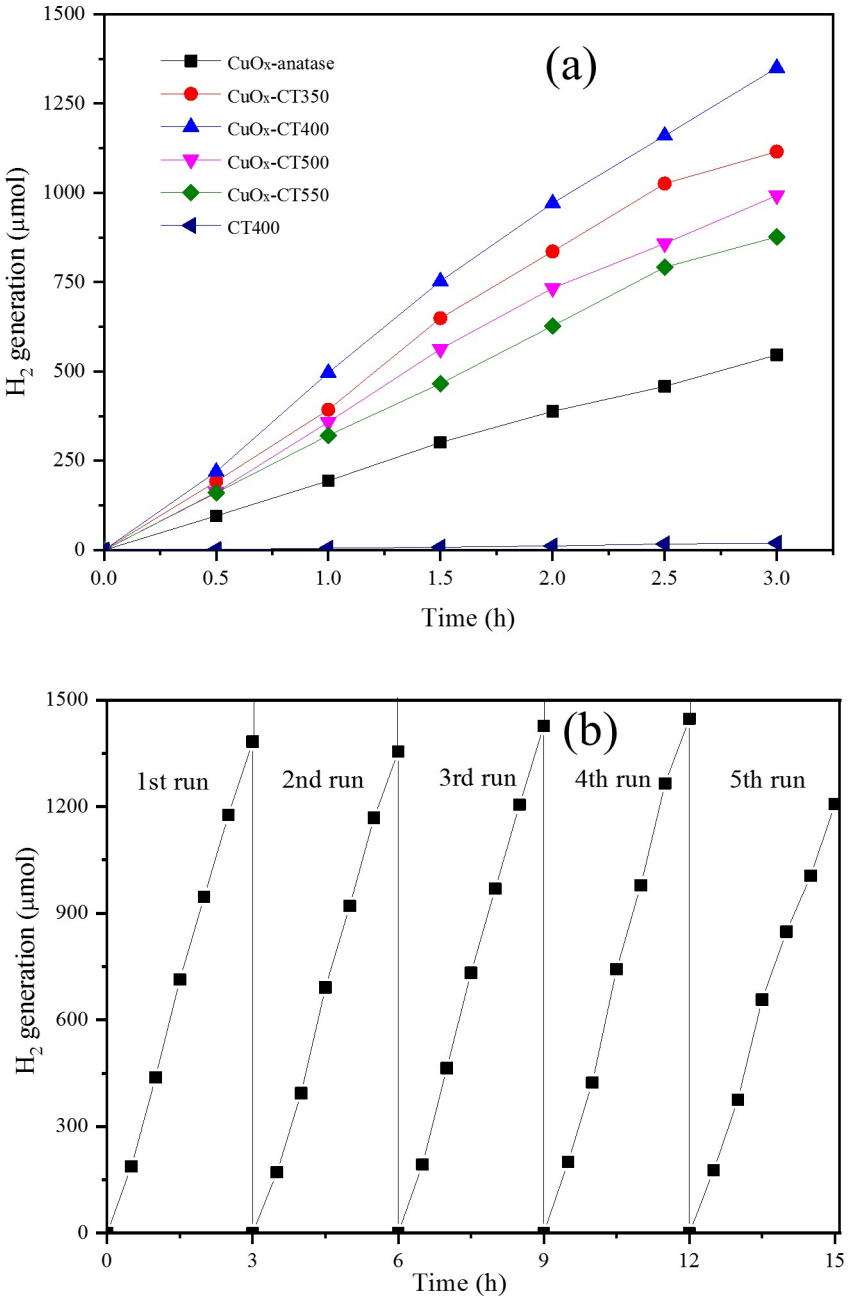

Fig 10. Photocatalytic activity experiment (a) and cycle experiment for CuO_x-CT400 (b).

https://doi.org/10.1371/journal.pone.0215339.g010

Fig 9B shows the Tafel spectra of both CT400 and CuO_x-CT400. Anode slope and corrosion current (j) are two major parameters of Tafel characterization. The anode slopes are 1.77 and 2.40 and the corrosion currents are 1.79 and 7.01 μA/cm^2 for CT400 and CuO_x-CT400, respectively. The larger anode slope and j values suggest the faster photoelectron transfer [46] of CuO_x-CT400, compared with CT400.

To further test the photoexcited charge carries transfer resistance of the catalyst, electrochemical impedance spectroscopy (EIS) [47] methods were used, and the results are shown in Fig 9C. The Nyquist spectra exhibit a high-frequency half-circle and a low-frequency straight

line, which is consistent with the reported literature. An equivalent circuit model shown in the image was constructed by ZsimpWin 3.10d based on the spectra. The model includes four parameters, R_{ct} (the reactivity resistance), R_s (the solution resistance), C_{dl} (double-layer capacitance), and Z_w (Warburg impedance), as shown in Table 1. Generally, R_{ct} indicates the resistance of the charge carrier transfer. Notably, R_{ct} values for CT400 (122 ± 1.69 Ω/cm^2) decreased to 80.6 ± 1.4 Ω/cm^2 for CuO_x-CT400. The result indicates that CuO_x modification significantly contributes to making the photoexcited charge carrier transfer more favorable and faster [48].

3.4 Photocatalytic activity

Fig 10A shows the photocatalytic hydrogen evolution of prepared samples under UV-visible light. The H_2 evolution amount follows the order of CuO_x-CT400 > CuO_x-CT350 > CuO_x-CT500 > CuO_x-CT550 > CuO_x-anatase > CT400. The CuO_x-CT400 catalyst exhibits a high hydrogen generation rate of 433.3 μmol/h, which reaches 56 times that of CT400 (7.7 μmol/h). CuO_x-anatase was prepared for comparison since it is difficult to prepare CuO_x-TiO_2 without carbon according to this method (the precursor $Ti(OBu)_4$ was both a carbon source and a titanium source). The H_2 evolution efficiency with CuO_x-anatase is 216.7 μmol/h, about half that of with CuO_x-CT400. The calcination temperature plays an important role for the H_2 generation of CuO_x-CTR catalysts. Generally, the higher temperature can result in higher crystallinity and lower carbonaceous material content of the catalyst. However, 400˚C is the optimal temperature indicating that crystallinity is not the main factor for the photoactivity. It can be speculated that carbon content and crystalline type are associated with photocatalytic H_2 generation.

The cycle experiment of the hydrogen evolution of CuO_x-CT400 is presented in Fig 10B. The H_2 generation is always high in the first four cycles and shows a little decrease in the 5th run.

The CO_2 and CO production of CT400 and CuO_x-CT400 are shown in Fig F in **S1** File. A significantly enhanced CO_2 and CO production rate was observed between CT400 and CuO_x-CT400, which is consistent with the H_2 evolution rate.

3.5 Mechanism

The results of the photoactivity experiment reveal that the carbon coated on the CuO_x-CT samples is important for the elevated photoactivity. However, the CT400 catalyst without Cu modification exhibited low photocatalytic efficiency. It seems reasonable to deduce that carbon materials could act as good electron conductors instead of proton reduction sites. Moreover, Joo et al. [49] prepared four different carbon-TiO_2 catalysts and concluded that electrically conductive carbon could only facilitate charge carries separation but made no direct contribution to the hydrogen formation. Further, in the synthesized materials, CuO_x species can be crucial co-catalysts which serve as both electron acceptor and surface redox reaction sites. Therefore, the carbonaceous material is speculated to act as an electron-bridge providing a new electron transfer channel from TiO_2 to the CuO_x species.

According to the results observed and discussed above, the probable mechanism of CuO_x modified C/TiO_2 for photocatalytic H_2 evolution featuring a synergistic effect of CuO_x and carbon is presented in Fig 11. Structurally, carbonaceous materials are coated on the TiO_2 surface through Ti-O-C bonds and CuO_x species can graft on both carbon materials and the TiO_2 surface. Electrons were photoexcited to the conduction band (CB) of TiO_2 with holes staying in the valence band (VB) under UV-visible light irradiation (Eqs 1 and 2). The electrons on the CB can go through two pathways. In pathway I, the electrons can be caught by the CuO_x

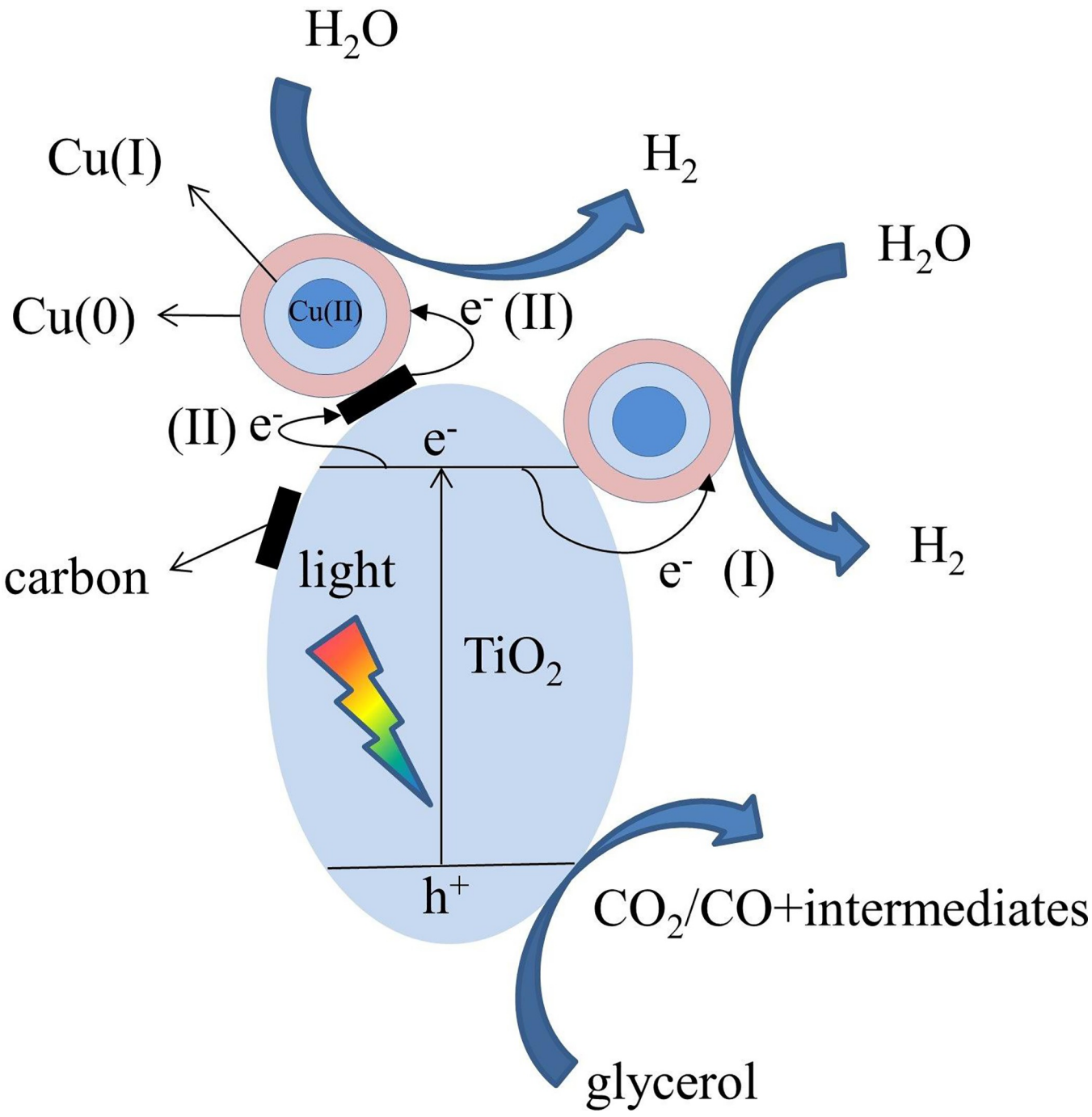

Fig 11. Photocatalytic hydrogen evolution mechanism of the CuO_x-C/TiO_2 catalyst with direct (I) and indirect (II) electron transport pathways.

https://doi.org/10.1371/journal.pone.0215339.g011

species to form Cu(I) or Cu(0), which results in efficient electron-hole separation (Eq 3). Meanwhile, CuO_x species can act as proton reduction reaction sites for hydrogen generation (Eq 4). In pathway II, the CB electrons first transfer to the carbon material and finally reach the CuO_x species. The new pathway enhanced the CuO_x effect as the co-catalyst by providing a new electron transfer route to promote the charge carrier separation.

Accordingly, the hydrogen evolution rate is significantly boosted by the synergistic effect of CuO_x and carbon materials over the CuO_x-C/TiO_2 catalyst. Glycerol could first be adsorbed onto the surface of TiO_2 and then was oxidized to CO_2, CO, and other intermediates ($C_2H_4O_2$, $C_2H_2O_3$, $C_2H_4O_3$, $C_3H_6O_3$, $C_3H_6O_4$, etc.) [22] by the photoexcited holes or hydroxyl radicals (Eqs 5 and 6).

$$\text{Catalyst} \xrightarrow{\text{light}} h^+_{VB} + e^-_{CB} \quad (1)$$

$$2H^+ + 2e^-_{CB} \rightarrow H_2 \quad (2)$$

$$Cu(II) + e^-_{CB} \rightarrow Cu(I)/Cu(0) \quad (3)$$

$$2Cu(I)/Cu(0) + 2H^+ \rightarrow 2Cu(II) + H_2 \quad (4)$$

$$h^+_{VB} + OH^- \rightarrow \bullet OH \quad (5)$$

$$\text{Glycerol} + h^+_{VB}/\bullet OH \rightarrow \text{intermediates} \rightarrow CO_2/CO + H_2O \quad (6)$$

4. Conclusion

Carbon coated on a TiO_2 surface modified with CuO_x has been prepared via a simple hydrolysis and photo-reduction method. With systematic structure characterization, carbonaceous materials were observed to be absorbed onto the surface of TiO_2 nanoparticles. The Cu species existed as CuO_x with multivalence states grafted both on the TiO_2 surface and the carbonaceous materials. With CuO_x functioning as a cocatalyst, the CuO_x-CTR exhibited high activities in photocatalytic hydrogen evolution. The photocatalytic hydrogen generation rate of the CuO_x-CT400 catalyst (433.3 μmol/h) is 56 times as high as that of CT400 (7.7 μmol/h). This significant increase is attributed to the synergistic effect between CuO_x and the carbon species. CuO_x grafted on the surface of the catalyst accepts photoexcited electrons inhibiting electron-hole recombination and serving as proton reduction sites. Meanwhile, carbonaceous materials function as good conductors by transferring electrons to the CuO_x, which significantly enhances the CuO_x co-catalyst effect. This work demonstrates a simple method to prepare a Cu and C co-modified TiO_2 catalyst with high photocatalytic performance and proposes the synergistic effect between copper and carbon, which presents a significant step in determining the photoexcited electron transfer mechanism.

Supporting information

S1 File. Table A in S1 File. Comparison of various TiO_2-based photocatalysts. **Fig A in S1 File.** SEM images of CT. **Fig B in S1 File.** TEM (a–c) and HRTEM (d) images of CT. **Fig C in S1 File.** SEM images of CT400. **Fig D in S1 File.** SEM images of CuO_x-CT400. **Fig E in S1 File.** Elemental mapping of CuO_x-CT400 (a-d) for C, Cu, O, and Ti. **Fig F in S1 File.** CO_2 (a) and CO (b) production of CT400 and CuO_x-CT400. Additionally, the raw data for figures has been uploaded to Figshare (http://dx.doi.org/10.6084/m9.figshare.7951724).
(DOCX)

Acknowledgments

Support from the National Natural Science Foundation of China (Grant No. 51278456 and 51778564) is gratefully acknowledged.

Author Contributions

Data curation: Xiuying Huang.

Formal analysis: Xiuying Huang, Meng Zhang.

Investigation: Xiuying Huang, Meng Zhang.

Methodology: Meng Zhang.

Supervision: Weirong Zhao.

Writing – original draft: Xiuying Huang, Runze Sun.

Writing – review & editing: Xiuying Huang, Gaoyuan Long, Yifan Liu.

References

1. Baykara SZ. Hydrogen: A brief overview on its sources, production and environmental impact. Int J Hydrogen Energy. 2018; 43(23):10605–14.
2. Dincer I, Acar C. Smart energy solutions with hydrogen options. Int J Hydrogen Energy. 2018; 43 (18):8579–99.
3. Sheikhbahaei V, Baniasadi E, Naterer GF. Experimental investigation of solar assisted hydrogen production from water and aluminum. Int J Hydrogen Energy. 2018; 43(19):9181–91.
4. Yu JX, Chen ZQ, Chen QQ, Wang Y, Lin HJ, Hu X, et al. Giant enhancement of photocatalytic H_2 production over $KNbO_3$ photocatalyst obtained via carbon doping and MoS_2 decoration. Int J Hydrogen Energy. 2018; 43(9):4347–54.
5. Rawool SA, Pai MR, Banerjee AM, Arya A, Ningthoujam RS, Tewari R, et al. pn Heterojunctions in NiO: TiO_2 composites with type-II band alignment assisting sunlight driven photocatalytic H_2 generation. Appl Catal, B. 2018; 221:443–58.
6. Singh R, Dutta S. A review on H_2 production through photocatalytic reactions using TiO_2/TiO_2-assisted catalysts. Fuel. 2018; 220:607–20.
7. Wu B, Liu D, Mubeen S, Chuong TT, Moskovits M, Stucky GD. Anisotropic Growth of TiO_2 onto Gold Nanorods for Plasmon-Enhanced Hydrogen Production from Water Reduction. J Am Chem Soc. 2016; 138(4):1114–7. https://doi.org/10.1021/jacs.5b11341 PMID: 26807600
8. Yuan YJ, Yu ZT, Li YH, Lu HW, Chen X, Tu WG, et al. A MoS_2/6,13-pentacenequinone composite catalyst for visible-light-induced hydrogen evolution in water. Appl Catal, B. 2016; 181:16–23.
9. Jiang W, Bai S, Wang L, Wang X, Yang L, Li Y, et al. Integration of Multiple Plasmonic and Co-Catalyst Nanostructures on TiO_2 Nanosheets for Visible-Near-Infrared Photocatalytic Hydrogen Evolution. Small. 2016; 12(12):1640–8. https://doi.org/10.1002/smll.201503552 PMID: 26833931
10. Luo M, Lu P, Yao W, Huang C, Xu Q, Wu Q, et al. Shape and Composition Effects on Photocatalytic Hydrogen Production for Pt–Pd Alloy Cocatalysts. ACS Appl Mater Inter. 2016; 8(32):20667–74.
11. Yoo J, Altomare M, Mokhtar M, Alshehri A, Al-Thabaiti SA, Mazare A, et al. Photocatalytic H_2 Generation Using Dewetted Pt-Decorated TiO_2 Nanotubes: Optimized Dewetting and Oxide Crystallization by a Multiple Annealing Process. J Phys Chem C. 2016; 120(29):15884–92.
12. Luna AL, Dragoe D, Wang K, Beaunier P, Kowalska E, Ohtani B, et al. Photocatalytic Hydrogen Evolution Using Ni–Pd/TiO_2: Correlation of Light Absorption, Charge-Carrier Dynamics, and Quantum Efficiency. J Phys Chem C. 2017; 121(26):14302–11.
13. Indra A, Menezes PW, Kailasam K, Hollmann D, Schroder M, Thomas A, et al. Nickel as a co-catalyst for photocatalytic hydrogen evolution on graphitic-carbon nitride (sg-CN): what is the nature of the active species? Chem commun. 2016; 52(1):104–7.
14. Xiong J, Liu Y, Liang S, Zhang S, Li Y, Wu L. Insights into the role of Cu in promoting photocatalytic hydrogen production over ultrathin HNb_3O_8 nanosheets. J Catal. 2016; 342:98–104.
15. Gu J, Yan Y, Young JL, Steirer KX, Neale NR, Turner JA. Water reduction by a p-$GaInP_2$ photoelectrode stabilized by an amorphous TiO_2 coating and a molecular cobalt catalyst. Nat mater. 2016; 15 (4):456–60. https://doi.org/10.1038/nmat4511 PMID: 26689139
16. Xiao S, Liu P, Zhu W, Li G, Zhang D, Li H. Copper Nanowires: A Substitute for Noble Metals to Enhance Photocatalytic H_2 Generation. Nano lett. 2015; 15(8):4853–8. https://doi.org/10.1021/acs.nanolett.5b00082 PMID: 26189663

17. Liu X, Zheng H, Sun Z, Han A, Du P. Earth-Abundant Copper-Based Bifunctional Electrocatalyst for Both Catalytic Hydrogen Production and Water Oxidation. ACS Catal. 2015; 5(3):1530–8.
18. Tian H, Zhang XL, Scott J, Ng C, Amal R. TiO_2-supported copper nanoparticles prepared via ion exchange for photocatalytic hydrogen production. J Mater Chem A. 2014; 2(18):6432–8.
19. Murakami N, Chiyoya T, Tsubota T, Ohno T. Switching redox site of photocatalytic reaction on titanium (IV) oxide particles modified with transition-metal ion controlled by irradiation wavelength. Appl Catal, A. 2008; 348(1):148–52.
20. Neubert S, Mitoraj D, Shevlin SA, Pulisova P, Heimann M, Du Y, et al. Highly Efficient Rutile TiO_2 Photocatalysts with Single Cu(II) and Fe(III) Surface Catalytic Sites. J Mater Chem A. 2016:Ahead of Print.
21. Nosaka Y, Takahashi S, Sakamoto H, Nosaka AY. Reaction Mechanism of Cu(II)-Grafted Visible-Light Responsive TiO_2 and WO_3 Photocatalysts Studied by Means of ESR Spectroscopy and Chemiluminescence Photometry. J Phys Chem C. 2011; 115(43):21283–90.
22. Zhang M, Sun R, Li Y, Shi Q, Xie L, Chen J, et al. High H_2 Evolution from Quantum Cu(II) Nanodot-Doped Two-Dimensional Ultrathin TiO_2 Nanosheets with Dominant Exposed {001} Facets for Reforming Glycerol with Multiple Electron Transport Pathways. J Phys Chem C. 2016; 120(20):10746–56.
23. Wang J, Wang Z, Zhu Z. Synergetic effect of $Ni(OH)_2$ cocatalyst and CNT for high hydrogen generation on CdS quantum dot sensitized TiO_2 photocatalyst. Appl Catal, B. 2017; 204:577–83.
24. Liu L, Liu Z, Liu A, Gu X, Ge C, Gao F, et al. Engineering the TiO_2–Graphene Interface to Enhance Photocatalytic H_2 Production. ChemSusChem. 2014; 7(2):618–26. https://doi.org/10.1002/cssc.201300941 PMID: 24323576
25. Xiang Q, Yu J, Jaroniec M. Enhanced photocatalytic H_2-production activity of graphene-modified titania nanosheets. Nanoscale. 2011; 3(9):3670–8. https://doi.org/10.1039/c1nr10610d PMID: 21826308
26. Woan K, Pyrgiotakis G, Sigmund W. Photocatalytic Carbon-Nanotube–TiO_2 Composites. Adv Mater. 2009; 21(21):2233–9.
27. Zhang H, Guo LH, Wang D, Zhao L, Wan B. Light-Induced Efficient Molecular Oxygen Activation on a Cu(II)-Grafted TiO_2/Graphene Photocatalyst for Phenol Degradation. ACS Appl Mater Interfaces. 2015; 7(3):1816–23. https://doi.org/10.1021/am507483q PMID: 25556692
28. Zhang M, Sun R, Long G, Zhou C, Zhou Y, Chen M, et al. Enhanced H_2 evolution of TiO_2 with efficient multiple electrons transfer modified by tiny CuO_x-NiO bimetallic oxides. Int J Hydrogen Energy. 2018; 43(17):8313–22.
29. Huerta-Flores AM, Torres-Martinez LM, Sanchez-Martinez D, Zarazua-Morin ME. $SrZrO_3$ powders: Alternative synthesis, characterization and application as photocatalysts for hydrogen evolution from water splitting. Fuel. 2015; 158:66–71.
30. Hafizah N, Sopyan I. Nanosized TiO_2 Photocatalyst Powder via Sol-Gel Method: Effect of Hydrolysis Degree on Powder Properties. Int J Photoenergy. 2009; 2009:8.
31. Zhao WR, Wang Y, Yang Y, Tang J, Yang YA. Carbon spheres supported visible-light-driven CuO-$BiVO_4$ heterojunction: Preparation, characterization, and photocatalytic properties. Appl Catal, B. 2012; 115:90–9.
32. Tuncel D, Okte AN. Efficient photoactivity of TiO_2-hybrid-porous nanocomposite: Effect of humidity. Appl Surf Sci. 2018; 458:546–54.
33. Dong F, Guo S, Wang H, Li X, Wu Z. Enhancement of the Visible Light Photocatalytic Activity of C-Doped TiO_2 Nanomaterials Prepared by a Green Synthetic Approach. J Phys Chem C. 2011; 115 (27):13285–92.
34. Zhang Y, Zhao Z, Chen J, Cheng L, Chang J, Sheng W, et al. C-doped hollow TiO_2 spheres: in situ synthesis, controlled shell thickness, and superior visible-light photocatalytic activity. Appl Catal, B. 2015; 165:715–22.
35. Deroubaix G, Marcus P. X-ray photoelectron spectroscopy analysis of copper and zinc oxides and sulphides. Surf Interface Anal. 1992; 18(1):39–46.
36. Peng Y, Shang L, Cao Y, Waterhouse GIN, Zhou C, Bian T, et al. Copper(i) cysteine complexes: efficient earth-abundant oxidation co-catalysts for visible light-driven photocatalytic H_2 production. Chem commun. 2015; 51(63):12556–9.
37. Zhao L, Chen X, Wang X, Zhang Y, Wei W, Sun Y, et al. One-Step Solvothermal Synthesis of a Carbon@TiO_2 Dyade Structure Effectively Promoting Visible-Light Photocatalysis. Adv Mater. 2010; 22 (30):3317–21. https://doi.org/10.1002/adma.201000660 PMID: 20574953
38. Zhong J, Chen F, Zhang J. Carbon-Deposited TiO_2: Synthesis, Characterization, and Visible Photocatalytic Performance. J Phys Chem C. 2010; 114(2):933–9.

39. Wu XY, Yin S, Dong Q, Guo CS, Li HH, Kimura T, et al. Synthesis of high visible light active carbon doped TiO_2 photocatalyst by a facile calcination assisted solvothermal method. Appl Catal, B. 2013; 142:450–7.

40. Zhong J, Chen F, Zhang J. Carbon-Deposited TiO_2: Synthesis, Characterization, and Visible Photocatalytic Performance. J Phys Chem C. 2010; 114(2):933–9.

41. Zhang H, Lv X, Li Y, Wang Y, Li J. P25-Graphene Composite as a High Performance Photocatalyst. Acs Nano. 2010; 4(1):380–6. https://doi.org/10.1021/nn901221k PMID: 20041631

42. Song L, Jing W, Chen J, Zhang S, Zhu Y, Xiong J. High reusability and durability of carbon-doped TiO_2/carbon nanofibrous film as visible-light-driven photocatalyst. J Mater Sci. 2019; 54(5):3795–804.

43. Yu J, Ran J. Facile preparation and enhanced photocatalytic H_2-production activity of $Cu(OH)_2$ cluster modified TiO_2. Energ Environ Sci. 2011; 4(4):1364–71.

44. Dong F, Wang H, Wu Z. One-Step "Green" Synthetic Approach for Mesoporous C-Doped Titanium Dioxide with Efficient Visible Light Photocatalytic Activity. J Phys Chem C. 2009; 113(38):16717–23.

45. Wang K, Li Q, Liu B, Cheng B, Ho W, Yu J. Sulfur-doped g-C_3N_4 with enhanced photocatalytic CO_2-reduction performance. Appl Catal, B. 2015; 176:44–52.

46. Meng C, Liu Z, Zhang T, Zhai J. Layered MoS_2 nanoparticles on TiO_2 nanotubes by a photocatalytic strategy for use as high-performance electrocatalysts in hydrogen evolution reactions. Green Chem. 2015; 17(5):2764–8.

47. Zheng D, Pang C, Liu Y, Wang X. Shell-engineering of hollow g-C_3N_4 nanospheres via copolymerization for photocatalytic hydrogen evolution. Chem commun. 2015; 51(47):9706–9.

48. Gondal MA, Li CL, Chang XF, Sikong L, Yamani ZH, Zhou Q, et al. Facile preparation of magnetic C/TiO_2/Ni composites and their photocatalytic performance for removal of a dye from water under UV light irradiation. J Environ Sci Heal A. 2012; 47(4):570–6.

49. Joo JB, Dillon R, Lee I, Yin Y, Bardeen CJ, Zaera F. Promotion of atomic hydrogen recombination as an alternative to electron trapping for the role of metals in the photocatalytic production of H_2. P Natl Acad Sci. 2014; 111(22):7942–7.